AIMS Materials Science, 13(5): 939–966.
DOI: 10.3934/matersci.2026044
Received: 05 July 2026
Revised: 16 September 2026
Accepted: 22 September 2026
Published: 26 October 2026

https://www.aimspress.com/journal/Materials

Research article

Molecular engineering of fluorinated benzodithiazole-based hole transport materials for efficient perovskite solar cells: A DFT study

Guannan Wang[1,†], Rani Sayyar[1,2,†], Tazeem Fatima[3], Sayyar Ali Shah[1,2,4,*], Ouyang Chun[2] and Aihua Yuan[1]

[1] School of Environmental & Chemical Engineering, Jiangsu University of Science and Technology, Zhenjiang 212003, PR China
[2] School of Materials Science & Engineering, Jiangsu University of Science and Technology, Zhenjiang 212003, PR China
[3] Department of Chemistry, University of Agriculture Faisalabad, 38000, Pakistan
[4] School of Medical Sciences, Shandong Xiehe University, Jinan, Shandong 250109, PR China

† These authors contribute equally to this work.

* **Correspondence:** Email: bilalsayyar70@gmail.com.

Abstract: Hole-transport materials (HTMs) are crucial for controlling charge dynamics in perovskite solar cells, particularly at the interface and during electron recombination. Here, a series of benzodithiazole (BBT) cores, linked to side-arm triphenylamine (TPA) groups and possessing a donor-π-donor architecture, was designed through molecular engineering with various fluorine substitutions on the core. The optoelectronic characteristics of the designed HTMs were investigated using the B3LYP and CAM-B3LYP/6-31G** methods within the density functional theory (DFT)/time-dependent DFT (TD-DFT) framework. All materials displayed energy gaps of 2.60–2.63 eV and absorption maxima at ~400 nm. Frontier molecular orbital (FMO) investigations demonstrated an efficient intramolecular charge transfer (ICT)from the BBT core to TPA donor arms. The transition density matrix maps and the density of states further supported the significant charge transfer. The fluorinated-designed HTMs exhibited lower exciton binding energies (E_b = 0.3423–0.3472 eV), resulting in higher exciton dissociation rates and enhanced charge transfer. A benchmark analysis using Spiro-OMeTAD (2,2,7,7-Tetrakis [N,N-di(4-methoxyphenyl)amino]-9,9-spirobifluorene) as a standard in HTM studies demonstrated that the engineered HTMs exhibited enhanced hole-transport performance. Photovoltaic performance of the designed HTMs was evaluated using Solar Cell

Capacitance Simulator in One Dimension (SCAPS-1D) device simulations. The optimized devices incorporating the designed HTM (BBT-F6) achieved a power conversion efficiency of up to 16%, outperforming the benchmark Spiro-OMeTAD under the same simulation conditions. These results indicate that structural modeling of organic HTMs with TPA donors can effectively tune their photovoltaic properties, making them promising candidates for efficient HTMs.

Keywords: hole-transport materials; density functional theory; benzodithiazole; SCAPS-1D; Spiro-OMeTAD; perovskite solar cells; fluorination

1. Introduction

Perovskite solar cells (PSCs) have emerged as leading candidates in next-generation photovoltaic technology. In contrast to conventional silicon-based cells, these systems offer lightweight construction, significant flexibility, and the potential for cost-effective, large-scale manufacturing [1–3]. Their molecular adaptability enables precise tuning of light absorption, energy level alignment, and charge transport. This combination of versatility and efficiency supports the development of high-performing, environmentally sustainable solar energy solutions [4,5].

In PSCs, the perovskite material acts as the primary light absorber. But the selection of transport materials remains critical for achieving optimal performance and long-term stability. Designing organic molecules that fulfill these functions effectively represents both a significant challenge and a promising avenue for advancing third-generation solar technologies [6,7]. High power conversion efficiencies (PCEs) in perovskite require careful selection of functional materials, particularly hole transport materials (HTMs). The HTM and PSCs serve as interfacial layers that selectively extract holes and block electrons, thereby minimizing recombination losses [5,8]. An ideal HTM must also be structurally stable, optically transparent, and have energy levels well matched to the adjacent layers [9,10].

Recently, many different materials have been used for these purposes [11,12]. Researchers have studied both organic and inorganic HTMs in detail. Some well-known organic HTMs include: poly(triarylamine) (PTAA) [13], Spiro-OMeTAD [14], poly(3,4-ethylenedioxythiophene): polystyrene sulfonate (PEDOT: PSS) [9], and poly(3-hexylthiophene) (P3HT) [15]. These materials can achieve high initial efficiency, but they also have drawbacks such as high cost, chemical instability, and complex deposition methods. PEDOT: PSS, because it is acidic and absorbs moisture, can corrode indium tin oxide (ITO) electrodes and damage nearby layers, which shortens device lifespan. On the other hand, inorganic HTMs such as MoOx [16] and NiO [17] are more heat and moisture-resistant, but they are often harder to process. In summary, designing new organic materials that are more stable, affordable, easy to make, and effective donors or HTMs across different solar cell designs is a promising yet difficult approach to improving third-generation solar technologies. Previously, we have investigated the optoelectonic and charge transfer properties of fluorinated benzothiadiazole-based derivatives for PSCs [18].

In this study, we have designed three novel HTMs, namely benzodithiazole with two fluorine (BBT-F2), benzodithiazole with four fluorine (BBT-F4), and benzodithiazole with six fluorine (BBT-F6), as shown in Figure 1. These materials incorporated benzodithiazole (BBT) as a central core, linked to two side arms bearing triphenylamine (TPA) donor groups. Fluorination is a technique for fine-tuning energy levels, especially by lowering the highest occupied molecular orbital (HOMO) to better align

it with the perovskite valence band, thereby enhancing charge-transfer efficiency. Additionally, fluorination has been shown to improve molecular packing, reduce energetic disorder, and increase film hydrophobicity, thereby enhancing charge extraction and operational stability in PSCs. In earlier studies on fluorinated cores and TPA-type HTMs, fluorine incorporation has been found to enhance interfacial charge extraction, morphology, and overall device performance, highlighting its importance in material design for PSC stability and efficiency.

For quantum calculations, we used density functional theory (DFT) and time-dependent DFT (TD-DFT) to BBT-based HTMs. Comparisons between DFT and TD-DFT calculations of the designed materials and Spiro-OMeTAD are made in this work to clarify the influence of fluorination on the electronic structure and charge-transfer characteristics associated with high-performance PSCs.

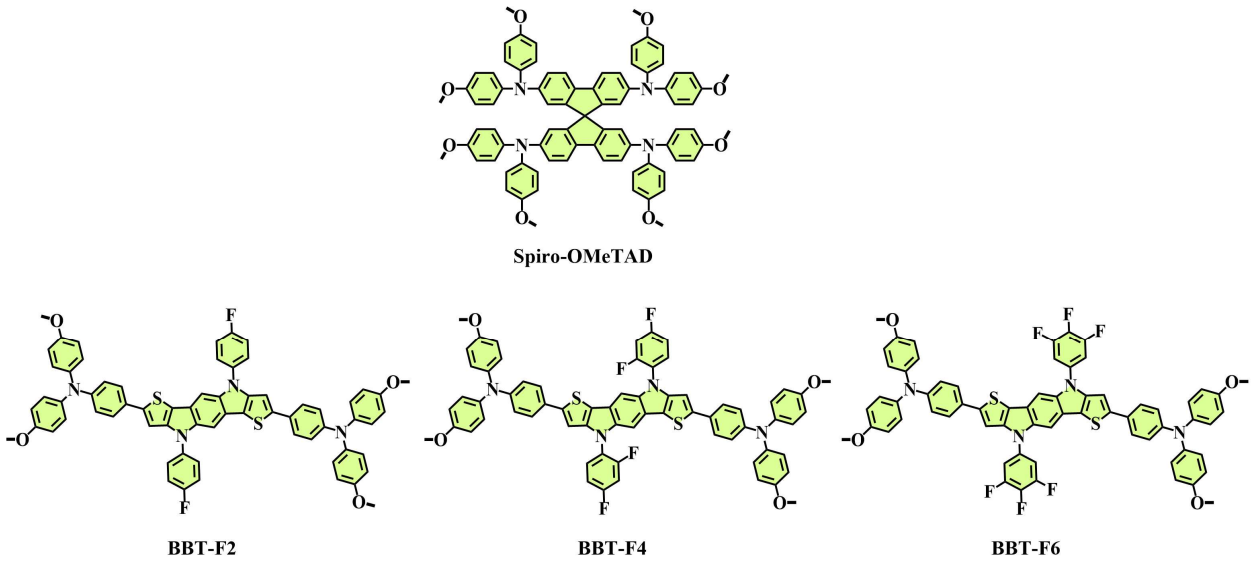


Figure 1. The chemical structures of Spiro-OMeTAD and fluorinated HTMs (BBT-F2, BBT-F4, and BBT-F6).

2. Materials and methods

All computational calculations were performed using the Gaussian 09 package, and the 3D molecular structures were designed using Gauss-View 6.0.16 [19]. The optimization of Spiro-OMeTAD and BBT-Fx (x corresponds to the number of F atoms in the designed BBT-HTM) series in their cation, anion, and neutral states was employed using the Becke Three-Parameter Lee–Yang–Parr B3LYP/6-31G** theory [20]. The B3LYP functional was chosen for its reliability in generating stable molecular structures, as evidenced by previous literature [21]. An implicit IEF-PCM model was used to calculate solvent effects using dichloromethane (CH_2Cl_2) [22]. TD-DFT calculations were performed using the long-range-corrected CAM-B3LYP functional [23] with 6-31G** basis set. We chose CAM-B3LYP because it more reliably predicts excitation energies and charge-transfer states than conventional DFT functionals [24,25]. The computational methodology and DFT parameters in this study adopted in this study are consistent with our previously reported procedures [18].

Hole-electron distribution (HED), charge density differences (CDD), and transition density matrix (TDM) heat maps were evaluated to study intramolecular charge transfer (ICT) in the first

singlet electronic excitation. The calculations have been performed using the CAM-B3LYP/6-31G** method [8] and processed with Multiwfn 3.8 [26]. Additionally, Gibbs free energies of solvation (ΔG_{sol}) were computed using the same theoretical method in the IEF-PCM solvation model using CH_2Cl_2 solvent to accurately describe the solvation effect [27].

The reorganization energies for electrons and holes in all designed molecules were calculated using the Eqs 1 and 2 below [28]:

$$\lambda_{electron} = [E^0(M^-) - E^0(M^0)] + [E^-(M^0) - E^-(M^-)] \quad (1)$$

$$\lambda_{hole} = [E^0(M^+) - E^0(M^0)] + [E^+(M^0) - E^+(M^+)] \quad (2)$$

where $\lambda_{\mathrm{electron}}$, λ_{hole} represent the reorganization energies for electrons and holes, respectively. Geometry relaxation causes this change in energy. M^+, M^-, and M^0 signify the optimized geometries of cation, anion, and neutral molecules, respectively. $E^0(M^-)$ represent the ground state energy of the anion, $E^0(M^0)$ is the ground-state energy for neutral molecules, $E^0(M^+)$ signifies the ground state energy of the cation, $E^+(M^0)$ represents the cationic energy of a neutral molecule, $E^+(M^+)$ is the cationic energy of the cation, $E^-(M^-)$ is the anionic energy of an anion, and $E^-(M^0)$ is the anion energy of a neutral molecule.

The ionization potential (IP) and electron affinity (EA) of the studied materials are calculated using the following Eqs 3 and 4 [29]:

$$IP = E^+(M^0) - E^0(M^0) \quad (3)$$

$$EA = E^0(M^0) - E^-(M^0) \quad (4)$$

3. Results

3.1. Electronic properties

In PSCs, the frontier orbital alignment between the perovskite absorber and the HTM is a central energetic requirement because it determines charge selectivity and interfacial recombination losses [30]. An effective HTM should provide a HOMO level positioned appropriately with respect to the perovskite valence band maximum (VBM) to enable efficient hole extraction, as well as a lowest unoccupied molecular orbitals (LUMO) level sufficiently higher than the perovskite conduction band minimum (CBM) to block electron transfer from the perovskite toward the metal electrode, thereby suppressing back electron injection and recombination. Within the same energetic framework adopted in the attached reference methodology, $CH_3NH_3PbI_3$ is typically described by VBM ≈ –5.43 eV and CBM ≈ –3.93 eV on the vacuum energy scale; hence, HTMs with HOMO levels above –5.43 eV and LUMO levels well above –3.93 eV are generally expected to support selective hole extraction while preventing electron leakage [31].

Accurate evaluation of the HTM HOMO is particularly important because the open-circuit voltage (Voc) is closely related to the energetic separation between the perovskite quasi-Fermi levels and the HTM contact. A deeper HOMO level is generally favorable for achieving a higher Voc, provided that interfacial hole extraction remains energetically feasible. However, the literature highlights that standard DFT calculations (notably B3LYP) tend to overestimate HOMO energies (i.e., predict them too shallow compared with experimental ionization energies/electrochemical HOMO values), which can lead to optimistic or inconsistent band-alignment conclusions if raw DFT HOMOs

are directly used [21,32]. To address this systematic deviation, the reference workflow employs an empirical fitting equation derived from a statistically meaningful set of experimentally validated HTMs, establishing a strong linear correlation between computed HOMO values ($HOMO^a$) and experimental HOMO values, and producing a calibrated HOMO ($HOMO^b$) shown in Eqs 5 and 6:

$$Y = 1.107x - 0.118 \tag{5}$$

where Y is the fitting HOMO energies, and x is the raw DFT-calculated HOMOs.

This correction was validated in the same study and found to be suitable for evaluating phenylamine-type HTMs, making it particularly relevant for our TPA-containing BBT series. To keep the electronic description consistent with that same literature workflow, LUMO levels are also estimated using the Eq 6:

$$(LUMO = HOMO^b + E) \tag{6}$$

where E is the first singlet excitation energy from B3LYP/TD-DFT. The optimized molecular structures of investigated HTMs is represented in Figure 2.

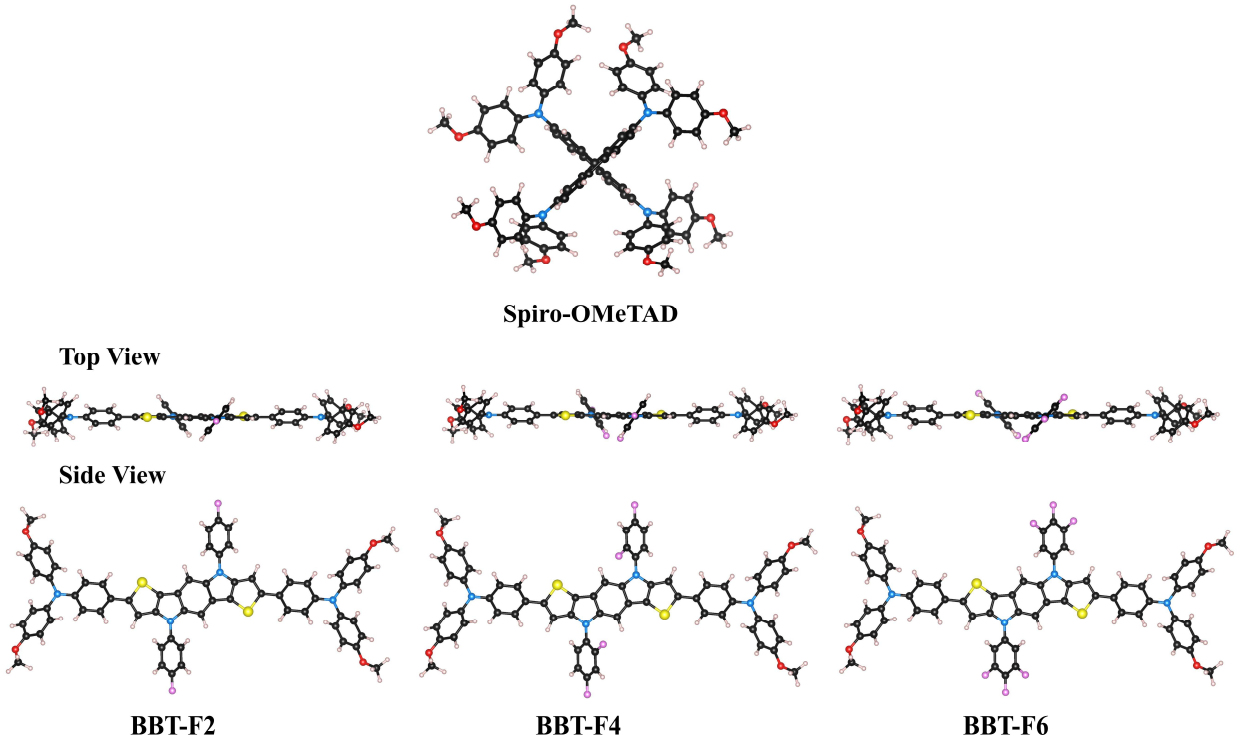


Figure 2. The optimized molecular structures of Spiro-OMeTAD, BBT-F2, BBT-F4, and BBT-F6 at B3LYP/6-31G** theory.

The electronic properties extracted for our designed HTMs are summarized in Table 1. For BBT-F2 and BBT-F4, the fitting HOMO values are identical ($HOMO^b$ = –4.89 eV), while the LUMO levels are –2.27 and –2.25 eV, respectively, yielding the same bandgap (E_{gap} = 2.63 eV). This near-overlap indicates that the change in fluorination degree between these two structures produces only a subtle perturbation in the frontier manifold within the fitted-HOMO framework. In contrast, BBT-F6 exhibits a clear stabilization of both frontier orbitals ($HOMO^b$ = –5.05 eV; LUMO = –2.45 eV) and a slightly

reduced band gap (2.60 eV), consistent with a stronger electron-withdrawing effect at higher fluorination. Importantly, BBT-F6 becomes energetically very close to the benchmark Spiro-OMeTAD in terms of HOMO.

Table 1. The DFT calculated HOMO (HOMO[a]), fitting HOMO (HOMO[b]), and fitting LUMO at B3LYP/6-31G** theory.

Compounds	HOMO[a] (eV)	HOMO[b] (eV)	LUMO (eV)	E_{gap} (eV)
BBT-F2	–4.31	–4.89	–2.27	2.63
BBT-F4	–4.31	–4.89	–2.25	2.63
BBT-F6	–4.46	–5.05	–2.45	2.60
Spiro-OMeTAD	–4.47	–5.07	–1.97	3.10

Considering the perovskite band edges, all three designed HTMs satisfy the key energetic conditions for selective contacts. Their fitted HOMO levels remain above the $MAPbI_3$ VBM level (−5.43 eV), supporting thermodynamically favorable hole transfer from the perovskite to the HTM. In comparison, their LUMO levels are substantially higher than the $MAPbI_3$ CBM (−3.93 eV), indicating effective electron-blocking behavior and reduced propensity for back-electron transfer and interfacial recombination. Within the BBT-Fx series, the progression from BBT-F2/BBT-F4 to BBT-F6 represents a shift toward a deeper HOMO.

Figure 3 shows the frontier molecular orbital diagram of Spiro-OMeTAD and the BBT-Fx series HTMs. In Spiro-OMeTAD, the HOMO and LUMO are mostly localized, which matches its bulky, non-flat structure that limits long-range π-conjugation. In comparison, BBT-F2, BBT-F4, and BBT-F6 have more spread-out orbitals along the BBT-TPA backbone. The HOMO is mainly found on the electron-rich TPA side arms and the nearby π-bridge, suggesting that hole formation is stabilized at the donor edges and that holes can move between molecules. The LUMO is focused on the electron-poor BBT core and its immediate surroundings, showing a clear donor-to-acceptor separation characteristic of intramolecular charge transfer. As fluorination increases from F2 to F6, the acceptor nature grows stronger: the LUMO becomes more centered on the core, while the HOMO stays mostly on the TPA units. This spatial arrangement helps with selective hole extraction and electron blocking, and the continuous orbital shapes suggest better electronic coupling than in Spiro-OMeTAD. Overall, the FMO analysis supports the idea that combining a fluorinated BBT core with TPA donors can improve charge separation and transport in the HTM layer. Also, the similar HOMO distributions across the series indicate that fluorination shifts energy levels without altering the main hole-transport path in the donor arms.

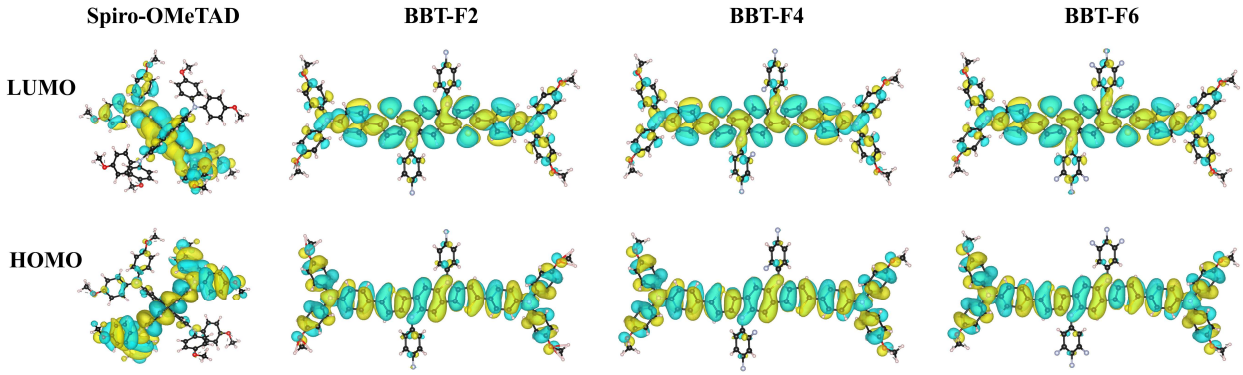


Figure 3. The distribution of HOMO and LUMO over molecular structures.

3.2. Photophysical properties

The ultraviolet-visible spectroscopy is more than a routine characterization step in PSCs: it directly informs how an HTM behaves optically within a full device stack. Modern lead-halide perovskites already exhibit strong absorption across the visible region, and device-level performance is typically optimized when charge-transport layers remain highly transparent over the perovskite's main harvesting window to minimize parasitic absorption and preserve photocurrent [33]. In addition, Ultraviolet–Visible (UV–Vis) trends (peak position, solvatochromic response, and oscillator strength) provide a convenient optical representation for the extent of π-conjugation and intramolecular charge-transfer character, which are frequently raised in recent HTM design studies to rationalize electronic structure and interfacial charge extraction [18]. Within this context, we analyzed the absorption maxima (λ_{max}) of the designed HTMs (BBT-F2, BBT-F4, and BBT-F6) in the gas phase and in two aromatic processing-relevant solvents, dichlorobenzene and chlorobenzene.

In the gas phase, BBT-F2, BBT-F4, and BBT-F6 absorb at 392.97, 391.59, and 393.33 nm, respectively, while Spiro-OMeTAD is blue-shifted at 381.4 nm. The ~11–12 nm blue shift of Spiro-OMeTAD is consistent with its more sterically constrained, non-planar architecture that typically limits effective conjugation compared with donor-acceptor (D-A) frameworks. In solution, the BBT-Fx series remains centered near ~400 nm: the λ_{max} observed in dichloromethane is 400.92, 399.68, and 400.74 nm for BBT-F2, BBT-F4, and BBT-F6, respectively; in chlorobenzene, it is 409.45, 400.66, and 401.82 nm. By contrast, Spiro-OMeTAD shows only a modest shift and remains at 389.57–389.86 nm in these solvents. From a device-stack viewpoint, maintaining the dominant HTM absorption in the near-UV/violet region (≈380–410 nm) is generally desirable, as it reduces overlap with the strongest perovskite absorption in the mid-visible range, where photocurrent is most sensitive. The photophysical parameters of studied HTMs in gas, dichloromethane (DCM), and chlorobenzene (CB) solvents are summarized in Table 2.

Table 2. The photophysical parameters of Spiro-OMeTAD, BBT-F2, BBT-F4, and BBT-F6 were calculated at a CAM-B3LYP/6-31G** level of theory.

HTMs	λ_{max} (nm)[a]	λ_{max} (nm)[b]	λ_{max} (nm)[c]	f[b]	f[c]	E_x (eV)[b]	E_x (eV)[c]
BBT-F2	392.97	400.92	409.45	2.89	2.85	3.09	3.03
BBT-F4	391.59	399.68	400.66	2.96	2.97	3.10	3.09
BBT-F6	393.33	400.74	401.82	2.95	2.97	3.09	3.09
Spiro-OMeTAD	381.40	389.57	389.86	1.09	1.12	3.18	3.18

Note: [a] UV–vis absorption (in nm) in gas phase. [b] UV–vis absorption (in nm), oscillator strength (*f*), and first excitation energy (E_x) in DCM. [c] UV–vis absorption, *f*, and first E_x in CB.

The solvent response of the absorption maxima further supports a stronger ICT component for the BBT-based HTMs than for Spiro-OMeTAD. Relative to the gas phase, BBT-F2 shifts by 7.95 nm in DCM and 16.48 nm in CB, while BBT-F4 shifts by 8.09 nm (DCM) and 9.07 nm (CB), and BBT-F6 shifts by 7.41 nm (DCM) and 8.49 nm (CB). Spiro-OMeTAD, in comparison, shifts by only 8.17 nm (DCM) and 8.46 nm (CB). Although both solvents are aromatic and relatively similar, the consistently larger bathochromic response of the BBT-Fx series indicates that the excited state is more polarizable and charge-transfer in nature, a trend widely discussed for donor-acceptor organic semiconductors where solvent stabilization amplifies ICT absorption (Figure 4). Importantly, fluorination shifts λ_{max} only slightly within the BBT family; instead, it fine-tunes over a narrow range, suggesting that the BBT-TPA conjugated motif dominates the transition energy, while F-content acts as a secondary electronic modulator. The additional short-wavelength band resolved in solution is attributed to solvent-induced changes in the relative stabilization and oscillator strength of higher-energy electronic transitions. Polarization of the molecular excited states by the continuum solvent can separate transitions that are weakly resolved in the gas-phase spectrum. The feature is therefore interpreted as an intensity-resolved higher-energy π–π*/locally excited (LE) transition rather than evidence for a new chemical species, while the dominant lower-energy band remains associated with the conjugated donor-acceptor framework.

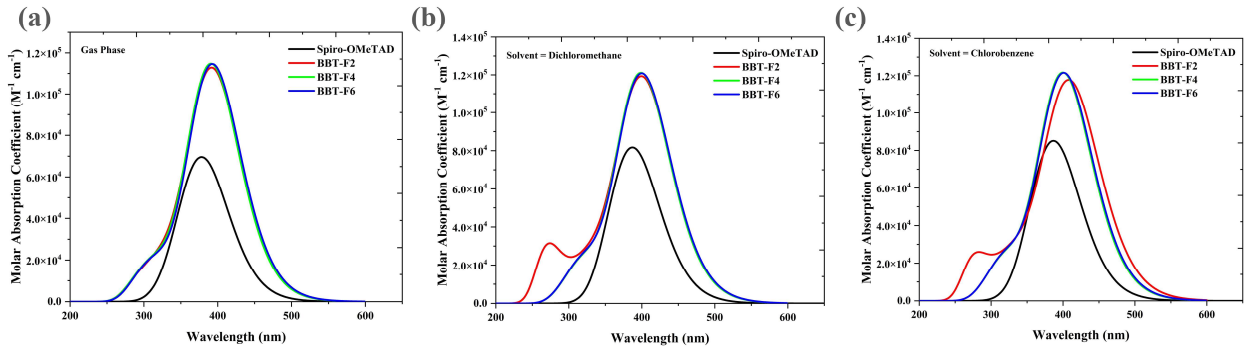


Figure 4. The UV–vis spectra of all studied materials: (a) in gas phase; (b) in solvent DCM; and (c) in solvent CB, were obtained at CAM-B3LYP/6-31G** theory.

The *f* values provide an additional performance-relevant contrast. The BBT-based HTM exhibits consistently high *f* values in both solvents (2.85–2.97), whereas Spiro-OMeTAD shows substantially

lower values (1.09–1.12). A higher *f* value indicates a more allowed and intense electronic transition, often due to stronger π–π* interactions and enhanced transition dipole moments in extended conjugated systems. These stronger transitions account for the more pronounced absorption features observed in the BBT-Fx series compared to Spiro-OMeTAD. However, their peak positions remain primarily in the near-UV region. Additionally, the exciton energies (E_x) are slightly lower for the BBT-Fx series than for Spiro-OMeTAD. For BBT-F2, BBT-F4, and BBT-F6, E_x values are 3.09, 3.10, and 3.09 eV in DCM, and 3.03, 3.09, and 3.09 eV in CB, respectively. Spiro-OMeTAD maintains an E_x of 3.18 eV in both solvents. This ~0.08–0.15 eV reduction indicates that the BBT-TPA framework is optically more accessible, consistent with a donor-acceptor motif that strengthens ICT relative to the spiro-linked reference. In practical PSC terms, these optical gaps remain sufficiently large to keep absorption largely away from the mid-visible, supporting the common goal of HTM transparency while still reflecting a conjugated, electronically responsive structure that can complement charge-extraction requirements at the perovskite interface.

3.3. Solubility and stability

The chemical stability of organic HTMs is essential for durable PSCs because perovskite absorbers are prone to degradation even under relatively low humidity, and interfacial processes can accelerate performance losses [8]. Alongside composition engineering and controlled fabrication, the HTM influences operational stability by affecting interfacial reactivity and mitigating photo-induced degradation pathways [34,35]. In this regard, global chemical reactivity descriptors (ionization potential, electron affinity, chemical hardness, softness, and Gibbs free energy) are widely used to estimate the intrinsic chemical stability of organic semiconductors. Photo-oxidation susceptibility can be linked to the energetic cost of forming the cation; hence, a higher IP generally indicates improved resistance to photo-induced oxidation.

Table 3 proposes the computed reactivity descriptors for the BBT-Fx series and compares them with Spiro-OMeTAD. The IP values of BBT-F2 (5.11 eV) and BBT-F4 (5.10 eV) are close to that of Spiro-OMeTAD (5.11 eV). BBT-F6 displays the highest ionization potential among all compounds within the series (5.22 eV). High IPs are favorable for oxidation resistance and, in turn, device stability. Higher IP for BBT-F6 can be understood as resulting from higher fluorination, which has a larger electron-withdrawing effect, stabilizing the closed-shell electronic structure while increasing the energetic cost of oxidized cation formation. Complementing this report of intrinsic stability, chemical hardness (η) was calculated [36]. Hardness values are widely used as an index of resistance to electronic perturbation. All BBT-Fx derivatives exhibit higher hardness values than Spiro-OMeTAD, which correlates with reduced chemical reactivity. Expectedly, chemical softness (S) values trend in the expected negative direction. The BBT-based HTMs showed reduced or equal softness (0.2021 eV) relative to Spiro-OMeTAD (0.22 eV). Taken together, these metrics indicate that fluorinated HTMs are intrinsically less polarizable and more chemically stable than Spiro-OMeTAD. Devices leveraging BBT-Fx could potentially have longer lifetimes due to improved stability.

To gauge how the solvation thermodynamics compare, Gibbs free energies were also compared in CH_2Cl_2 using the Eq 7:

$$(\Delta G_{sol} = \Delta G_{DMSO} - \Delta G_{gas}) \tag{7}$$

Here, ΔG_{CH2Cl} and ΔG_{gas} are the single-point energies in the solvent (CH_2Cl_2) and gas phases, respectively [22]. We find that the BBT-Fx compounds possess lower ΔG_{sol} than Spiro-OMeTAD and display negative values in dimethyl sulfoxide (DMSO) (Table 3). Furthermore, the EA values of the BBT-Fx series are quite low (0.43–0.61 eV) when compared to Spiro-OMeTAD (1.09 eV). Since EA is typically associated with an electron-accepting character, these results suggest that fluorination does not induce an undesirable increase in n-like character; rather, these materials are dominated by hole-transporting behavior. BBT-F2 and BBT-F4 have oxidation stability similar to that of Spiro-OMeTAD. At the same time, they outperform BBT-F6 by showing higher oxidation potential and greater chemical hardness, along with higher intensity and lower softness.

Table 3. Ionization potential, electron affinity, chemical hardness, softness, and solvation free energy of studied HTMs.

Compounds	IP (eV)	EA (eV)	η (eV)	S (eV)	ΔG (kcal mol^{-1})
BBT-F2	5.11	0.45	4.87	0.21	–19.05
BBT-F4	5.10	0.43	4.88	0.20	–16.76
BBT-F6	5.22	0.61	4.92	0.20	–16.43
Spiro-OMeTAD	5.11	1.09	4.56	0.22	–15.92

The molecular electrostatic potential (Figure 5a) provides a rapid assessment of the surface charge distribution [37]. In Spiro-OMeTAD, the potential is patchy and predominantly localized at the molecular edges, indicating uneven polarization. Within the design series, the BBT core and adjacent heteroatom regions exhibit stronger negative potential (red-orange). In contrast, the donor-rich TPA arms display more positive potential (green-blue), consistent with a donor-acceptor electronic structure. Increasing fluorine substitution renders the core more electron-deficient and amplifies the potential difference between the BBT core and TPA regions. This enhanced polarization facilitates directional charge transfer and promotes selective interfacial interactions.

3.4. Density of states (DOS)

DOS analysis provides a direct way to rationalize how electronic states are distributed near the frontier region and, more importantly, which molecular fragments contribute more strongly to the occupied (HOMO) and unoccupied (LUMO) manifolds. The occupied states correspond to the HOMO-related region, and the unoccupied states correspond to the LUMO-related region, while fragment (projected) DOS is used to quantify how different subunits control the frontier levels and to infer charge-transfer character from donor/core partitioning [38,39]. Using the same interpretation, our projected DOS results (Table 4) clearly distinguish the electronic roles of the BBT core and the donor (TPA) arms in BBT-F2, BBT-F4, and BBT-F6, and benchmark them against Spiro-OMeTAD. To probe intramolecular charge transfer, each structure was divided into two fragments: the central core (red) and the terminal donor unit (blue). The black trace represents the total DOS contribution from the whole molecule (Figure 5b). As summarized in Table 4, a clearer and more systematic trend emerges for the LUMO region. Across the BBT-Fx series, the LUMO is predominantly core-centered (69%–72%), with donor contributions remaining minor (28%–31%). Specifically, the core contribution is 69.5% for BBT-F2 and 69.1% for BBT-F4, increasing to 72.3% for BBT-F6. This

indicates that the electron-deficient BBT core mainly governs the unoccupied frontier manifold, and the slight increase in core share from F2/F4 to F6 supports the expected strengthening of acceptor character with increasing fluorination. Such a donor-acceptor partitioning is a hallmark DOS signature of ICT, consistent with efficient charge separation under operation. Spiro-OMeTAD shows a strongly donor-dominated HOMO (66.5%) and an even more core-dominated LUMO (84.4%), indicating a spatial separation of frontier character. Compared to Spiro-OMeTAD, the BBT-Fx series retains a core-dominated LUMO while exhibiting a more distributed HOMO. Overall, the DOS results verify core control over the LUMO and shift the HOMO toward the donor TPA, thereby supporting a rationale donor-acceptor electronic motif relevant to hole transport.

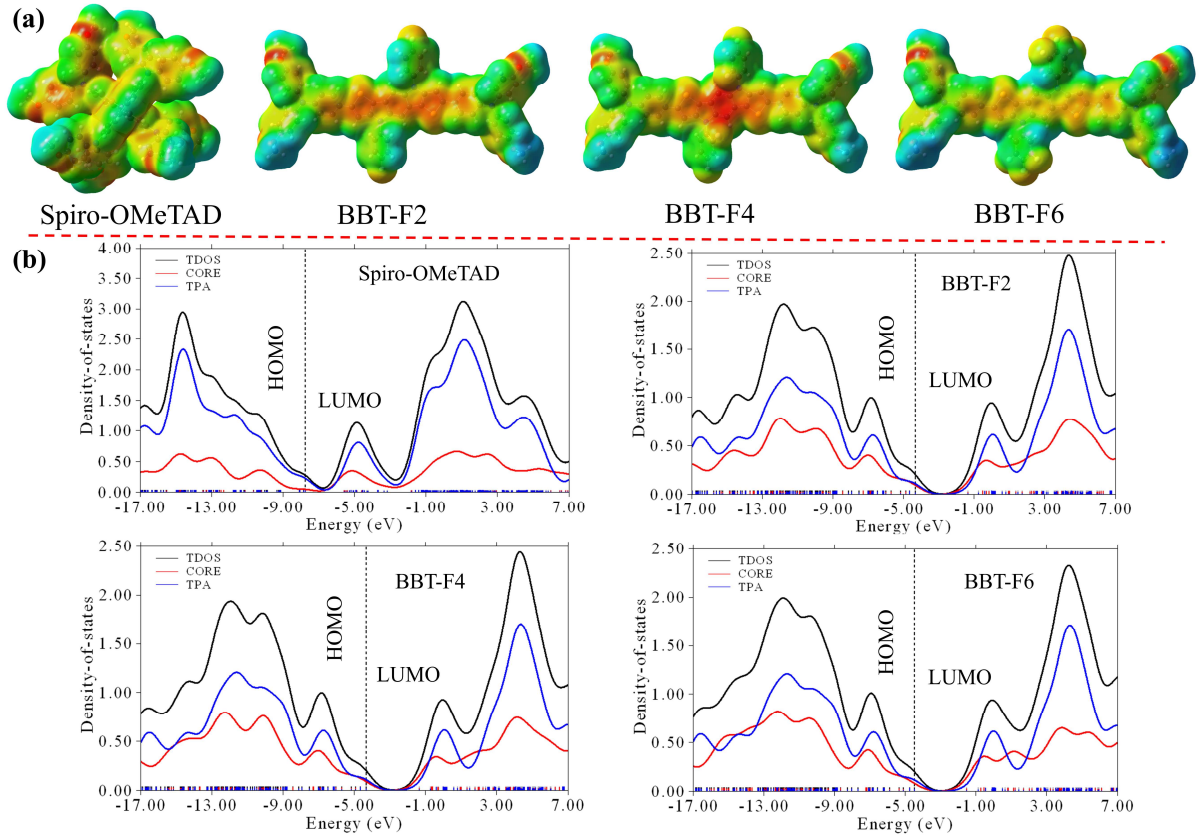


Figure 5. (a) Molecular electrostatic potential maps. (b) DOS graphs for the studied molecules via the electronic state population method.

Table 4. The percentage of core and donor in HOMO and LUMO.

Compounds	HOMO		LUMO	
	Core (%)	Donor (%)	Core (%)	Donor (%)
BBT-F2	52.3	47.7	69.5	30.5
BBT-F4	51.5	48.6	69.1	30.9
BBT-F6	43.0	57.0	72.3	27.7
Spiro-OMeTAD	33.5	66.5	84.4	15.6

3.5. Transition density matrix

The lowest first singlet excitation (S_1) was characterized using TDM analysis to measure the extent of coherence between electrons and holes and the extent of charge transfer within the intramolecular system in the studied HTMs [40]. The TDM maps (Figure 6) were generated by subdividing each molecule into two fragments: the electron-deficient core (C) and the peripheral donor units (D). In this representation, locally excited (LE) contributions confined to an individual fragment are mostly found in the diagonal blocks (C→C and D→D), and donor-core charge-transfer coupling can be found in the off-diagonal blocks (C↔D). In the BBT-Fx series, the transition density is mainly concentrated in the C→C block, and the intensity is evident and continuous as it extends into the C→D block. This correlation shows that there is a mixed excitation with a π–π* character that prevails in the conjugated backbone, which is accompanied by a significant ICT contribution, owing to an effective donor-acceptor electronic communication. In comparison, Spiro-OMeTAD exhibits a more rambling transition-density distribution and relatively lower off-diagonal strength, which is in line with a more localized excitation and smaller D-A coherence.

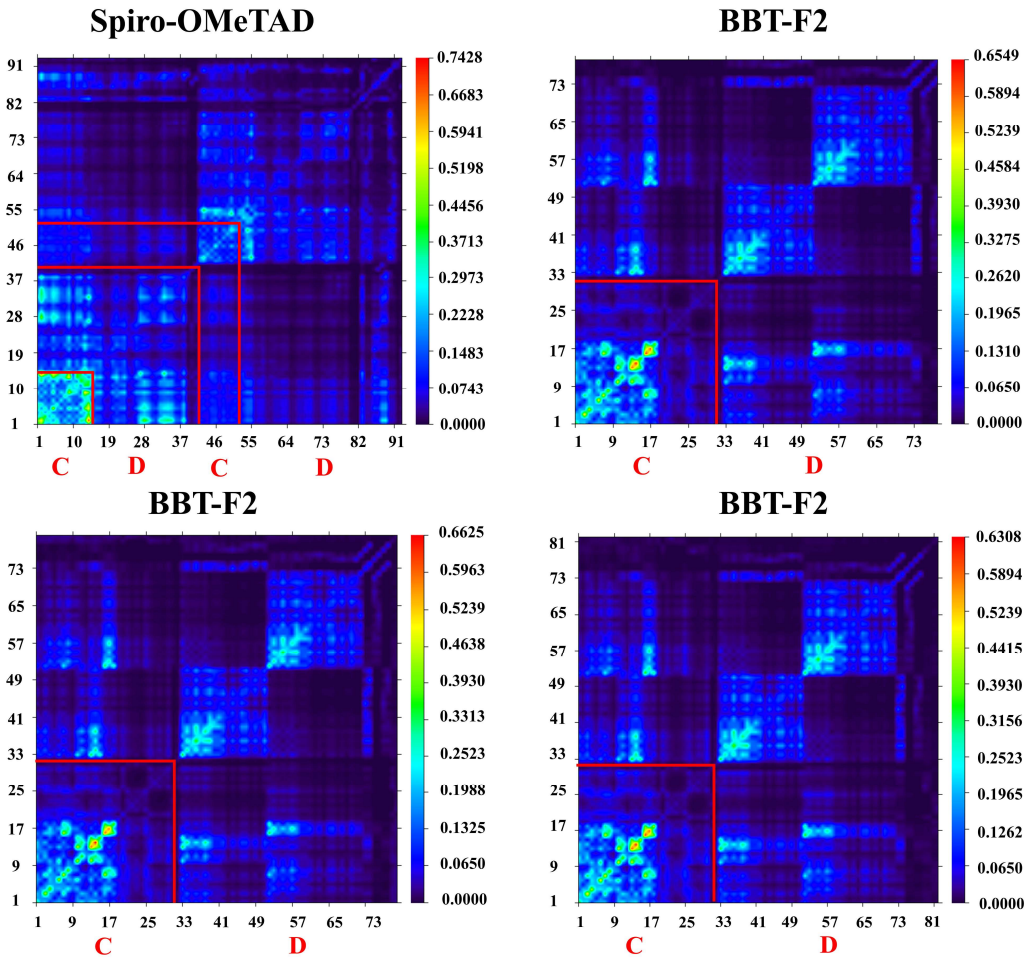


Figure 6. Transition-density heat maps of Spiro-OMeTAD and all designed BBT-Fx HTMs.

The observed TDM features are consistent with the FMO and projected DOS analyses, which indicate that the HOMO is primarily associated with the donor arms. At the same time, the LUMO is

preferentially localized on the core. Collectively, these findings support directional charge redistribution upon photoexcitation and further validate the donor-acceptor design rationale for fluorinated BBT-based HTMs.

3.6. Excitation binding energy

Another key parameter that determines the optoelectronic behavior of organic charge-transport layers is the exciton (electron-hole) binding energy (E_b). Lower E_b values are generally favored because weaker Coulomb attraction allows the photoexcited electron-hole pair to separate, enabling more efficient charge production and transport [29]. In the current series, the designed HTMs exhibit low binding energies of 0.3462 (BBT-F2), 0.3472 (BBT-F4), and 0.3423 eV (BBT-F6). These values are also very low compared to those of Spiro-OMeTAD (0.7625 eV), corresponding to a reduction of about 0.42 eV and revealing much weaker electron-hole coupling in the BBT-based model. The binding energy values are listed in Table 5.

This decrease in E_b is in line with the D-A nature of the BBT-TPA structure. Spatial separation of the frontier electronic states is more favorable for intramolecular charge-transfer contributions and increases the effective electron-hole distance, thereby reducing the Coulomb binding energy. The small variation observed within the BBT-Fx series further implies that fluorination modulates electronic energetics while preserving uniform exciton binding strength. Among the three compounds, BBT-F6 exhibits the lowest E_b, indicating the most favorable charge separation within the designed HTMs.

Table 5. Calculated exciton E_b for all studied HTMs.

HTMs	E_g (eV)	E_x (eV)	E_b (eV)
BBT-F2	2.97	2.62	0.3462
BBT-F4	2.98	2.63	0.3472
BBT-F6	2.94	2.60	0.3423
Spiro-OMeTAD	3.86	3.09	0.7625

3.7. Reorganization energy and charge transfer rates

The interactions between molecular relaxation determine the charge-transport rates in HTMs during oxidation/reduction and electronic coupling between neighboring molecules, which collectively determine the rate of hole transfer as defined by the semi classical Marcus theory [41–43]. In the present study, the BBT-Fx series illustrates relatively low and comparable λ_{hole} values of 0.2576 (BBT-F2), 0.2470 (BBT-F4), and 0.2290 eV (BBT-F6), all of which are similar to that of Spiro-OMeTAD (0.2476 eV) (Table 6). This implies that BBT-F6 has an intrinsic transport advantage over molecular reorganization. Conversely, all the compounds (0.4867–0.4974 eV for BBT-Fx, 0.3256 eV for Spiro-OMeTAD) exhibit larger electron reorganization energies, consistent with the hole-selective behavior of these HTMs, as inhibited electron transport may reduce interfacial recombination.

The electronic coupling descriptors, however, introduce an important distinction within the series. BBT-F2 and BBT-F4 show comparatively large hole transfer integrals (t_{hole} = 0.17), translating into very high hole transfer rates (k_{hole}) of 7.79×10^{13} and 8.82×10^{13}, respectively. These k_{hole} values exceed those of Spiro-OMeTAD (4.85×10^{12} s^{-1}) by roughly an order of magnitude, indicating

markedly stronger electronic communication and faster hopping kinetics in the BBT-F2/BBT-F4 HTMs (Table 6). Although BBT-F6 has the lowest λ_{hole}, its coupling is significantly smaller (t_{hole} = 0.04 eV), resulting in a lower k_{hole} (6.04×10^{12} s^{-1}) that is only moderately higher than Spiro-OMeTAD. This shows that intermolecular coupling dominates the rate trend: strong t_{hole} in BBT-F2/F4 outweighs its slightly higher λ_{hole}, whereas weaker coupling in BBT-F6 limits its hopping rate despite a favorable reorganization energy. Practically, this suggests that BBT-F2 and BBT-F4 are more promising for high intrinsic hole mobility, provided that their solid-state packing supports the calculated dimer geometry. At the same time, BBT-F6 may require morphology/packing optimization to translate its low λ_{hole} into superior macroscopic transport.

Finally, the maximum amount of charge transfer (ΔN_{max}) provides insight into the extent of electron density displacement during charge migration [44]. The BBT-Fx series shows ΔN_{max} values of 1.023*e* (BBT-F2), 1.019*e* (BBT-F4), and 1.060*e* (BBT-F6), compared with 1.047*e* for Spiro-OMeTAD (Table 6). The consistently ~1.0 magnitude indicates substantial charge-transfer character across all HTMs. At the same time, the slightly larger ΔN_{max} for BBT-F6 suggests the most pronounced charge displacement within the designed series, consistent with stronger D-A polarization at higher fluorination. Taken together, these results demonstrate that the BBT-Fx platform combines competitive hole-transport descriptors relative to Spiro-OMeTAD. BBT-F2 and BBT-F4 deliver the strongest electronic coupling and fastest hole-hopping rates, whereas BBT-F6 exhibits the lowest hole reorganization energy and the largest charge-transfer amplitude, highlighting a tunable balance between intermolecular coupling, structural relaxation, and charge-transfer strength in fluorinated BBT-based HTMs.

Table 6. Reorganization energy for hole (RE_{hole}), electron reorganization energy ($RE_{electron}$), t_{hole}, k_{hole}, and ΔN_{max} of all HTMs.

Compounds	λ_{hole} (eV)	$\lambda_{electron}$ (eV)	t_{hole} (eV)[a]	k_{hole} (s^{-1})[b]	ΔN_{max} (e)[c]
BBT-F2	0.2576	0.4974	0.17	7.79×10^{13}	1.023
BBT-F4	0.2470	0.4867	0.17	8.82×10^{13}	1.019
BBT-F6	0.2290	0.4937	0.04	6.04×10^{12}	1.060
Spiro-OMeTAD	0.2476	0.3256	0.04	4.85×10^{12}	1.047

Note: [a] $t_{hole} = \frac{1}{2}(E_{HOOMO} - E_{HOMO-1})$. Calculations based on Koopmans' energy-splitting-in-dimer theorem. [b] $k_{hole/electron} = \frac{2\pi}{h} \frac{t^2_{(hole/electron)}}{\sqrt{4\pi\lambda_{hole/electron} K_B T}} \exp -(\frac{\lambda_{hole/electron}}{4K_B T})$, where K_B is the Boltzmann constant, h is the Plank's constant, and t is the transfer integral for hole and electron. The k_{hole} is affected by λ_{hole} and t_{hole}. ΔN_{max} is calculated using following equation [45]: [c] $\Delta N_{max} = -\frac{\text{Chemical potential}}{\text{Chemical hardness}}$.

3.8. Excitation analysis

Electron-excitation descriptors such as the integral of hole, integral of electron, hole-electron spatial extension index (H-index), hole-electron separation index (t-index), hole-electron spatial extension along the charge-transfer direction (HCT), the hole delocalization index and electron delocalization index (HDI and EDI) provide a quantitative analysis of how the excited-state electron-hole pair is distributed in space, how strongly charge transfer (CT) is involved, and how delocalized the generated hole and electron densities become after excitation. In general, larger t-index magnitudes

indicate stronger hole-electron spatial separation. On the other hand, higher charge-transfer metric (H_CT) values reflect a larger CT contribution. Larger HDI and EDI indicate broader delocalization of the hole-electron density, which can benefit exciton dissociation and suppress localized recombination pathways [40,46].

Both carriers in the BBT-Fx series have almost identical hole and electron integrals (0.927–0.936), which give rise to a balanced hole-electron formation and similar transition probabilities in both channels. The integrals of Spiro-OMeTAD are slightly larger (0.964/0.964), indicating a slight improvement in the total strength of excitation. Nonetheless, integrals alone are inferior to identifying the localization of charge transfer in the excitation. Spatial indices reveal more distinct differences. BBT-Fx HTMs show much higher values of H-index (6.37–6.62 Å) as compared to the Spiro-OMeTAD (4.95 Å), which is an indication of a well-defined hole-electron distribution and a stronger spatial redistribution after excitation. The t-index of BBT-F2, BBT-F4, and BBT-F6 is negative and high in value (−6.19, −6.29, and −5.98 Å), and Spiro-OMeTAD has a significantly low t-index (−1.61 Å). This difference shows that BBT-Fx excitations exhibit significantly greater charge separation than Spiro-OMeTAD, indicating a more directional donor-acceptor excitation in the fluorinated BBT motif. Moreover, H_CT is about two times higher in BBT-Fx (6.16–6.42 Å) than in Spiro-OMeTAD (3.10 Å), which is a direct sign of a more significant role of the charge-transfer component in the new HTMs. These results indicate that BBT-Fx materials can improve charge separation in photovoltaic devices.

The delocalization indices also provide further insight into charge separation. The BBT-Fx series is found to have HDI values of 4.11–4.22 with EDI values of 4.22–4.33, which are slightly less than those of Spiro-OMeTAD (HDI = 4.51; EDI = 4.93). This implies that excited-state hole-electron densities are more widely spread over its molecular framework in Spiro-OMeTAD. Overall, the increased t-index and higher H_CT values indicate that BBT-Fx promotes electron-hole separation, while Spiro-OMeTAD shows greater delocalization and reduced charge-transfer separation. This difference is important for PSC interfaces because the more charge-transfer nature of BBT-Fx is associated with a higher rate of exciton dissociation and slower Coulomb binding, reflected in lower binding energies. However, even in moderate delocalization, charge migration remains possible provided intermolecular coupling is present.

BBT-F4 has the largest H-index (6.62 Å) and H_CT (6.42 Å) and the lowest t-index (−6.29 Å), suggesting a strong charge-transfer division. Conversely, BBT-F6 has slightly lower H_CT (6.16 Å) and H-index (6.37 Å), but the highest HDI and EDI values in the series (4.22 and 4.33, respectively), indicating a milder increase in delocalization. Taken together, these excitation descriptors indicate that the fluorinated BBT-based HTMs exhibit more intense charge-transfer excitations than Spiro-OMeTAD. This observation is consistent with a D-A design that enhances charge separation and can minimize recombination losses at the perovskite–HTM interface. The electron excitation descriptors are listed in Table 7.

Table 7. Electron excitation indices of all designed HTMs.

Compounds	Hole integral	Electron integral	H-index (Å)	t-index (Å)	H_CT (Å)	HDI	EDI
BBT-F2	0.930	0.930	6.51	−6.19	6.32	4.16	4.24
BBT-F4	0.927	0.927	6.62	−6.29	6.42	4.11	4.22
BBT-F6	0.936	0.936	6.37	−5.98	6.16	4.22	4.33
Spiro-OMeTAD	0.964	0.964	4.95	−1.61	3.10	4.51	4.93

3.9. Hole-electron distribution and charge density difference

The HED analysis is a quantitative method that separates hole-electron densities by fragment, enabling clear evaluation of charge separation and electron-hole overlap, which are the focus of exciton dissociation [47]. The CDD strategy provides a graphical representation of electron depletion and accumulation following excitation, indicating the direction and magnitude of intramolecular charge transfer. In Figure 7, the excited-state charge redistribution is directly shown and observed at the fragment and domain levels by combining CDD iso-surfaces with the percentage contribution of holes, electrons, and their overlap on the core and TPA fragments, making it useful for interpreting aspects of charge transfer.

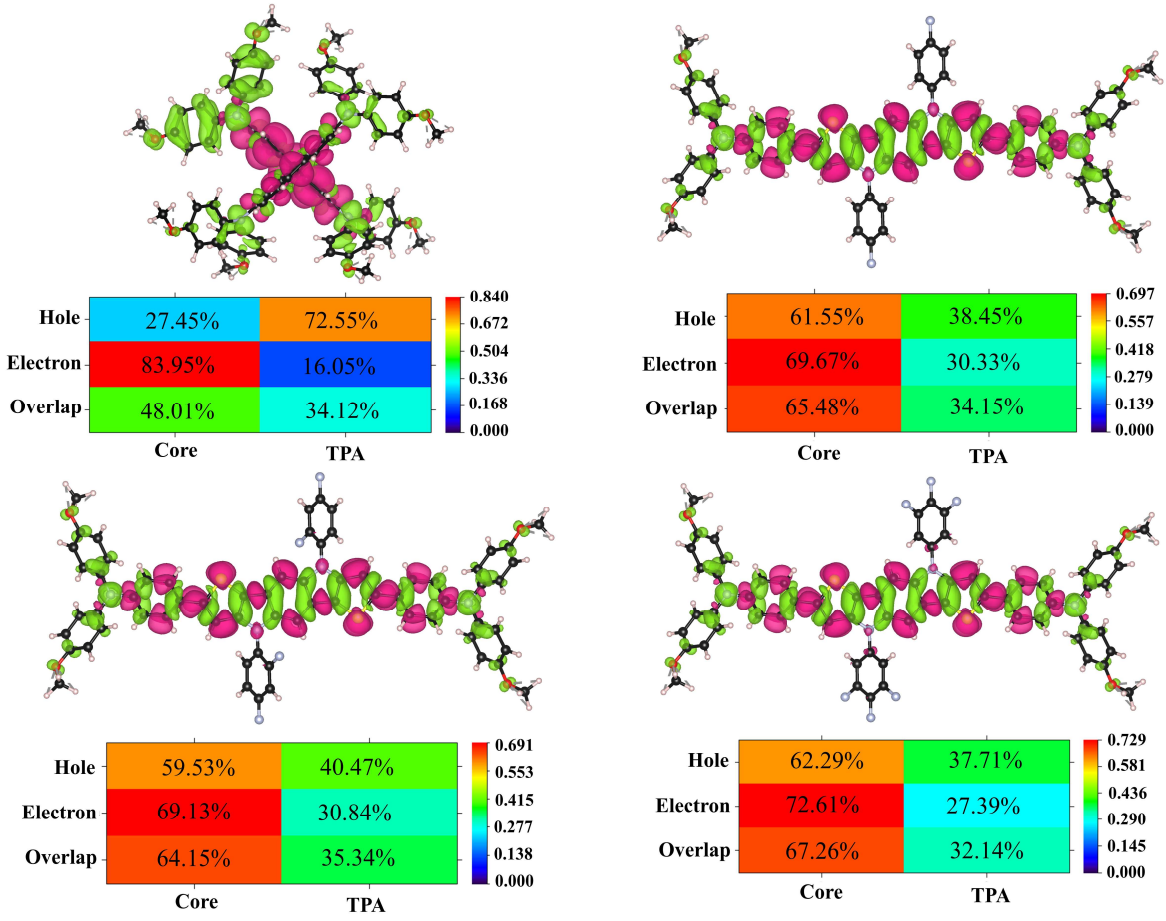


Figure 7. Charge density difference surfaces (red color represents the electron-rich site, and green color represents the electron depletion area) and hole-electron distribution heat maps with percentage contributions to spatial charge generation and overlap.

Spiro-OMeTAD has the strongest donor-acceptor separation. The central core (83.95%) and TPA donor arms exhibit strong electron and hole localization, respectively. This pronounced separation underscores the directional nature of ICT in this system, thereby emphasizing the robustness of the charge-transfer signature. This specific behavior is further supported by the overlap values (core 48.01%, TPA 34.12). The BBT-Fx series, in contrast, has a more core-dominated excitation. In the case of BBT-F2, BBT-F4, and BBT-F6, the contribution of the hole is in the core (61.55%, 59.53%, and 62.29%),

and the electron is still core-centered (69.67%, 69.13%, and 72.61%). This will lead to an increased percentage of overlap on the core (65.48%, 64.15%, and 67.26%), suggesting greater electron-hole co-localization and an improved π–π* component of the conjugated backbone, plus a medium ICT contribution from the TPA side arms. BBT-F6 shows the highest core overlap and the highest core electron share, suggesting a more core-confined excited state, while BBT-F4 shows the greatest TPA involvement in the hole (40.47%). This suggests slightly enhanced donor participation. Overall, Spiro-OMeTAD presents the strongest fragment-separated ICT. At the same time, BBT-F2/F4/F6 favor mixed local excitation with partial ICT, where both the electron and a significant portion of the hole reside on the core. The CDD iso-surfaces reinforce these quantitative trends by visually depicting where electron density is depleted and accumulated upon excitation, consistent with the different degrees of charge separation inferred from the fragment percentages.

3.10. Hirshfeld analysis

Hirshfeld surface (HS) analysis was employed to visualize and compare the intermolecular contact environment of the BBT-Fx series in a packing-sensitive manner, complementing the electronic descriptors by identifying the types and spatial distributions of short contacts that can govern solid-state organization. The 3D-Hirshfeld of investigated HTMs are generated using the Crystal Explorer 17.5 software. The HS mapped over normalized contact distance (d_{norm}) highlights regions where intermolecular separations are shorter, comparable, or longer than the sum of van der Waals radii (Figure 8a) [48]. In the d_{norm} surfaces of BBT-based HTMs, the dominant coloration is white to light blue, indicating that most contacts lie near or above van der Waals distances (i.e., weak dispersive contacts) [49,50]. Importantly, BBT-F2 displays more clearly apparent localized red features and a negative d_{norm} minimum (−0.126 Å), which is typically indicative of relatively stronger contacts at specific sites (often weak C–H···X, C–H···π, or sulfur/fluorine influenced contacts depending on the functional groups) [51]. In contrast, BBT-F4 and BBT-F6 show comparatively fewer intense red hotspots and positive d_{norm} minima, consistent with a contact landscape dominated by nonspecific dispersive interactions and fewer pronounced short-contact regions. This qualitative shift suggests that increasing fluorination tends to redistribute the close-contact regions rather than forming strong localized hydrogen-bond motifs, which aligns with the expectation for largely π-conjugated HTMs, where packing is often governed by dispersion, C–H···π, and π–π interactions.

To further probe π-driven recognition, HS maps over shape index were analyzed. The shape-index surfaces (Figure 8b) for all three BBT-Fx compounds exhibit alternating red and blue patches distributed across the conjugated backbone. Such complementary patterns are typically associated with surface concave/convex features arising from close π-contacts (including π···π and C–H···π interactions) and indicate that molecular surfaces can form face-to-face or offset stacking motifs rather than purely edge-to-edge contacts. Notably, BBT-F4 and BBT-F6 show more continuous and frequent red and blue patching along the central region compared to BBT-F2, implying that higher fluorination may enhance the surface complementarity needed for recurring π-associated contacts, even if those contacts do not manifest as highly localized red d_{norm} hotspots.

The curvedness analysis (Figure 8c) provide an additional packing descriptor by distinguishing flat from highly curved regions. Across the designed series, the curvedness maps show broad green areas over the molecular core, consistent with relatively flat surface patches that can support π-stacking. Among the three, BBT-F6 presents slightly larger, smoother low-curvedness domains along the

backbone, suggesting a greater propensity for sustained planar contact regions that may benefit intermolecular electronic coupling when favorable stacking occurs. BBT-F2 appears more segmented in low-curvedness continuity, consistent with a packing environment where close contacts are more site-specific rather than broadly distributed across an extended planar patch.

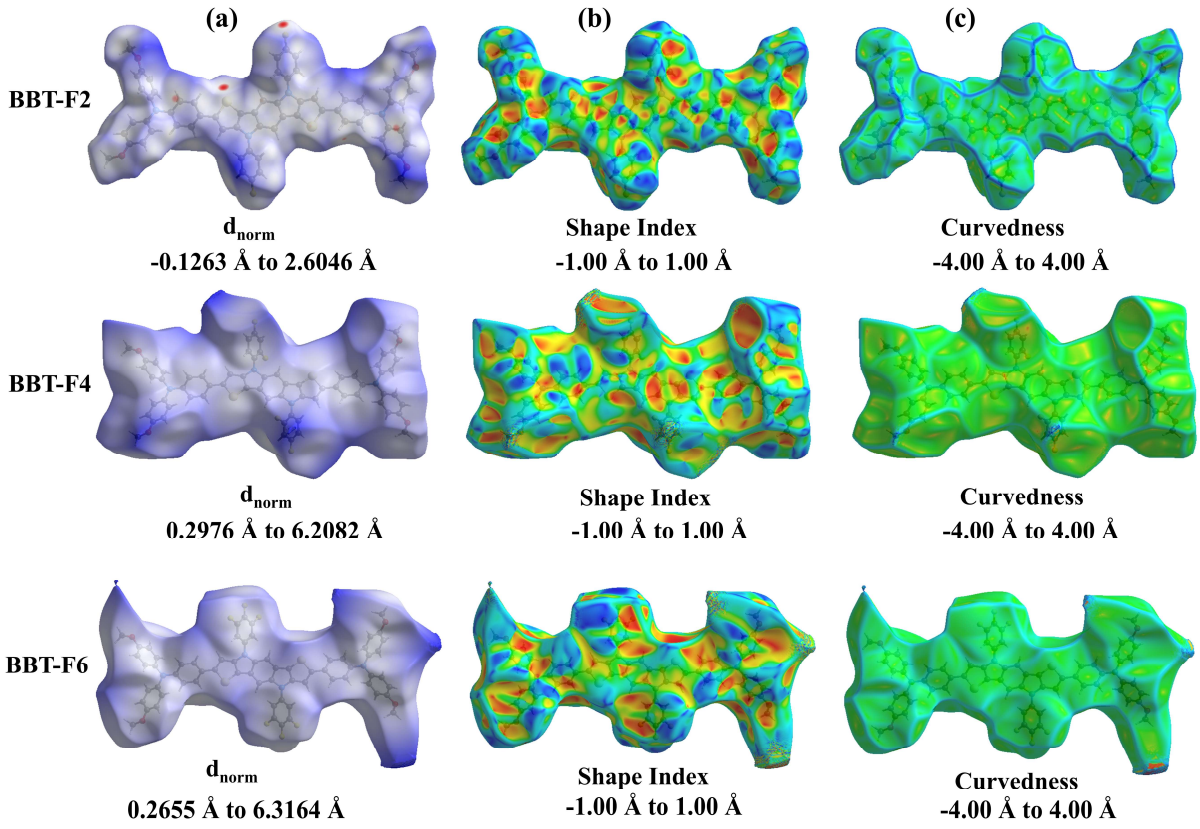


Figure 8. (a) Hirshfeld plots of d_{norm}, (b) shape index, and (c) curvedness for the Spiro-OMeTAD and BBT-Fx series.

The Hirshfeld 2D fingerprint plots (Figure 9) provide a compact signature of the dominant intermolecular contacts controlling solid-state packing. In these maps, sharp spikes or distinct wings at low (di/de) indicate relatively short, specific contacts, whereas broader diffuse regions reflect mainly dispersive interactions [52]. For the BBT HTMs, fingerprints consistently show prominent H···C/C···H wings, characteristic of C–H···π (and related H···C) contacts, confirming that dispersion-assisted π-surface interactions are a key packing motif across all three HTMs. A discernible C···C region is also evident, supporting the presence of π···π-associated contacts between conjugated backbones. Comparing the series, BBT-F2 displays clear H···C/C···H features along with noticeable C···C contributions, and additional minor regions attributable to heteroatom contacts (e.g., O- or F-involving interactions). In BBT-F4, fluorine-related features become more defined, with more visible H···F/C···F contact regions while maintaining strong H···C/C···H and C···C signatures. BBT-F6 retains dominant H···C/C···H and C···C contributions, indicating that fluorination primarily refines and redistributes the contact topology rather than introducing an entirely new interaction type. Overall, the fingerprint plots complement the HS surfaces by confirming persistent π-driven packing with increasing participation of F-involving contacts as fluorination increases.

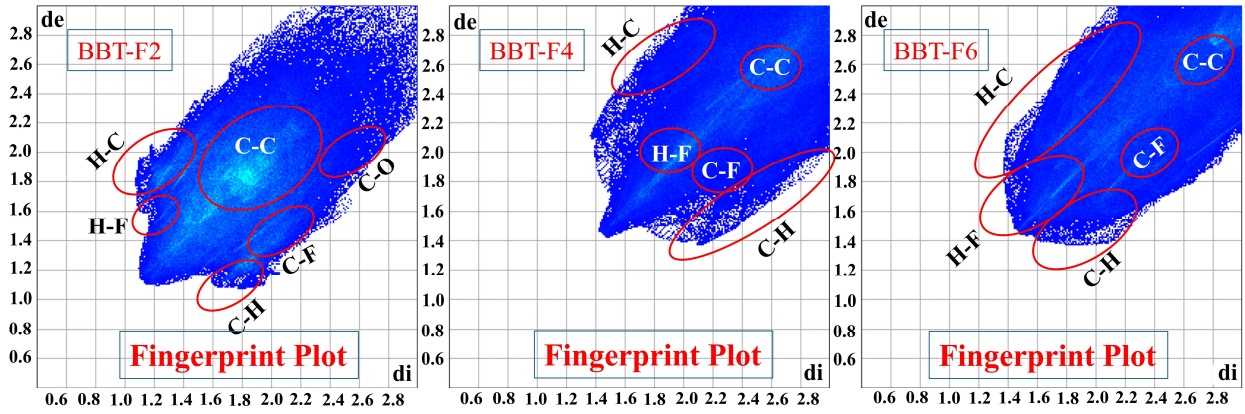


Figure 9. Fingerprint plots displaying the major proportion of intermolecular contact.

Overall, the HS results indicate that the BBT-Fx HTMs are largely stabilized by dispersive and π-associated contacts, with BBT-F2 showing more pronounced localized short-contact signatures, while BBT-F4 and BBT-F6 exhibit a more uniformly distributed π-contact-compatible surface. This qualitative trend supports the structure-packing rationale that fluorination can modulate the contact topology and thereby influence the solid-state organization relevant to charge-transport behavior.

3.11. Device simulation using SCAPS-1D

The photovoltaic response of the designed BBT-Fx HTMs was assessed using SCAPS-1D and benchmarked against a conventional Spiro-OMeTAD device [53]. To keep the comparison transparent and reproducible, all layer thicknesses and electrical parameters (e.g., permittivity, carrier mobilities, and related transport inputs) were adopted directly from literature sources, so that differences in output can be discussed in the context of the HTM design rather than parameter fitting. The SCAPS simulation parameters such as thickness (t), bandgap (E_g), electron affinity (χ), relative dielectric permittivity (ε_r), effective density of states in the conduction band (N_c), effective density of states in the valence band (N_v), electron mobility (μ_e), hole mobility (μ_h), donor density (N_D), acceptor density (N_A), total defect density (N_T) are listed in Table 8. The simulated n-i-p semiconductor stack consisted of TiO_2 (20 nm)/$MAPbI_3$ (550 nm)/HTM, where the BBT-Fx layers were 200 nm thick and the Spiro-OMeTAD reference layer was 150 nm thick. $MAPbI_3$ was used as the photoactive perovskite absorber. The complete electrical parameters of each layer are provided in Table 8. The identical μ_h values assigned to the BBT-Fx layers in SCAPS-1D are a controlled literature-based assumption rather than values derived directly from the Marcus hopping rates. k_{hole} is a microscopic dimer-level hopping descriptor, whereas SCAPS requires an effective bulk-film mobility that additionally depends on packing, energetic disorder, trap states, and film morphology. In the absence of experimentally measured or rigorously upscale mobilities for the newly designed compounds, direct proportional scaling of μ_h from k_{hole} would not be physically justified. Consequently, the SCAPS calculations are interpreted as a comparative device-level analysis under a common mobility baseline, while the molecule-specific k_{hole} values are discussed separately as intrinsic transport descriptors.

Table 8. Different structural and electronic parameters used for SCAPS-1D simulation for the solar cell architecture.

Parameters	TiO_2	$MAPbI_3$	BBT-F2	BBT-F4	BBT-F6	Spiro-OMeTAD
t (nm)	20	550	200	200	200	150
E_g (eV)	3.20	1.5	2.63	2.63	2.60	2.88
χ (eV)	3.90	3.93	2.27	2.25	2.45	2.05
ε_r	9	30	3	3	3	3.0
N_c	1.0×10^{21}	2.5×10^{20}	2.8×10^{21}	2.8×10^{21}	2.8×10^{21}	2.5×10^{18}
N_v	1.0×10^{19}	2.5×10^{20}	2.8×10^{21}	2.8×10^{21}	2.8×10^{21}	2.5×10^{18}
μ_e	20	50	2.3×10^{-5}	2.3×10^{-5}	2.3×10^{-5}	2.1×10^{-3}
μ_h	10	50	2.7×10^{-4}	2.7×10^{-4}	2.7×10^{-4}	2.6×10^{-3}
N_D	1.0×10^{18}	0	0	0	0	0
N_A	0	1.0×10^{15}	1.0×10^{18}	1.0×10^{18}	1.0×10^{18}	1.0×10^{18}
N_T	1.0×10^{14}	1.0×10^{15}	1.0×10^{15}	1.0×10^{15}	1.0×10^{15}	1.0×10^{15}
References	[54]	[55,56]	[57–59]			

Under these consistent conditions, the simulated metrics show that BBT-F6 delivers the best performance (PCE = 16.60%), essentially matching Spiro-OMeTAD (16.44%), while BBT-F2 (13.34%) and BBT-F4 (12.92%) are lower (Table 9). A notable feature of the dataset is the near-identical short-circuit current density (J_{SC}) for all devices (25.56–25.57 mA cm^{-2}). This is fully consistent with the overlapping external quantum efficiency (EQE) spectra, where the same wavelength response and cutoff are obtained regardless of the HTM. Figure 10a represents the voltage versus current density whereas Figure 10b presents the simulated EQE curves for BBT-F2, BBT-F4, BBT-F6, and Spiro-OMeTAD. The curves nearly overlap because the perovskite absorber and optical-generation profile were kept unchanged, which is consistent with the nearly identical JSC values obtained for all four devices. Since the absorber and optical generation profile are unchanged in the simulations, the HTM does not introduce an optical penalty here. Instead, the performance differences are primarily controlled by Voc and fill factor (FF), which reflect recombination and charge-selectivity at the perovskite–HTM interface. Within the BBT series, the main separation is in voltage: BBT-F2 and BBT-F4 show lower Voc values (0.78 and 0.76 V), whereas BBT-F6 reaches 0.93 V, exceeding Spiro-OMeTAD (0.89 V). This trend aligns well with the molecular-level approach. BBT-F6 has a deeper, Spiro-like fitting HOMO, which strengthens energetic compatibility for hole extraction while reducing the probability of interfacial back transfer, thereby lowering recombination losses. In the same direction, the excitation analysis (DOS, TDM and hole-electron distribution) indicates that the BBT framework supports donor-acceptor electronic communication, and the reduced exciton binding energy relative to Spiro suggests a weaker electron–hole Coulomb coupling; both factors can facilitate charge separation and limit recombination pathways at operating bias. The device ranking cannot be inferred from a single molecular descriptor. Because JSC remains essentially unchanged, the PCE difference is governed mainly by Voc and FF. BBT-F6 reaches the highest Voc (0.93 V) and a competitive FF (69.47%), consistent with its deeper fitted HOMO (−5.05 eV) and more favorable interfacial energetic alignment. By contrast, BBT-F2 and BBT-F4 show the highest microscopic k_{hole} values, indicating strong intrinsic hopping kinetics, but this advantage is not directly propagated into the SCAPS simulations because a common literature-derived μ_h was used for the BBT layers. Accordingly, BBT-F6 is the best candidate

under the present device-model assumptions, whereas BBT-F2/F4 remain attractive where intrinsic hole-hopping kinetics are prioritized.

Table 9. Computed photovoltaic properties via SCAPS-1D for the Spiro-OMeTAD and BBT-Fx series.

HTMs	Voc (V)	J_{SC} (mA cm^{-2})	FF (%)	PCE (%)
BBT-F2	0.78	25.56	66.86	13.34
BBT-F4	0.76	25.56	66.43	12.92
BBT-F6	0.93	25.57	69.47	16.60
Spiro	0.89	25.56	71.57	16.44

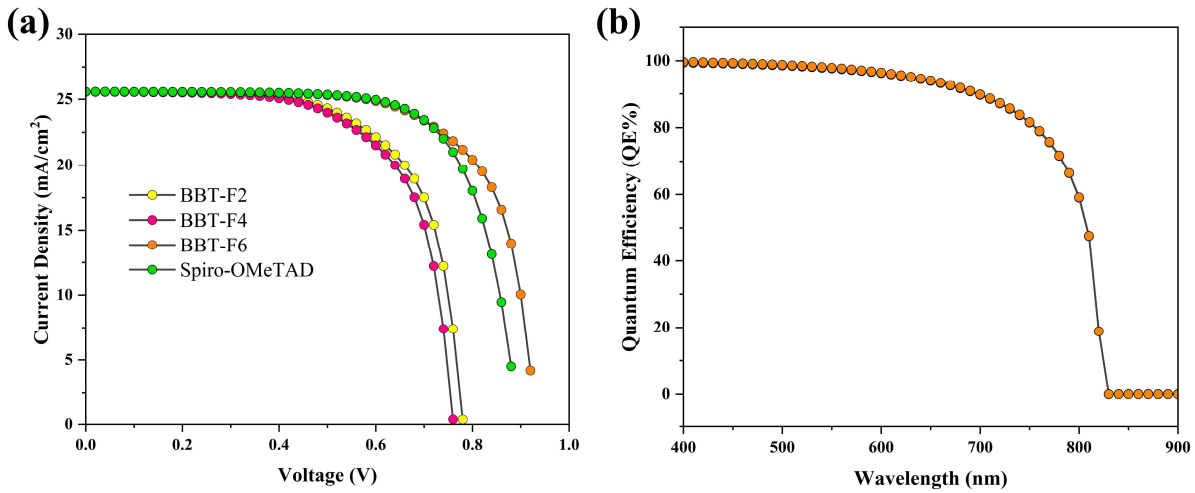


Figure 10. (a) The current density-voltage (J-V) curves and (b) quantum efficiency vs. wavelength of BBT-Fx series and Spiro-OMeTAD.

Within the BBT series, the main separation is in voltage: BBT-F2 and BBT-F4 show lower Voc values (0.78 and 0.76 V), whereas BBT-F6 reaches 0.93 V, exceeding Spiro-OMeTAD (0.89 V). This trend aligns well with the molecular-level approach. BBT-F6 has a deeper, Spiro-like fitting HOMO, which strengthens energetic compatibility for hole extraction while reducing the probability of interfacial back transfer, thereby lowering recombination losses. In the same direction, the excitation analysis (DOS, TDM and hole-electron distribution) indicates that the BBT framework supports donor-acceptor electronic communication, and the reduced exciton binding energy relative to Spiro suggests a weaker electron–hole Coulomb coupling, both factors that can facilitate charge separation and limit recombination pathways at operating bias.

The FF follows a similar flow. Spiro-OMeTAD retains the highest FF (71.57%), while BBT-F6 remains competitive (69.47%), supporting its high PCE. In contrast, BBT-F2 and BBT-F4 display lower FF values (66.86 and 66.43%) and their J-V curves bend earlier (Figure 10a), which is typically linked with stronger recombination or less favorable charge selectivity in the forward-bias region. Overall, the SCAPS results indicate that the designed HTMs do not change photocurrent generation (consistent EQE and J_{SC}), but they strongly influence voltage and FF losses. Among them, BBT-F6 emerges as the most promising candidate, achieving near-Spiro device performance by improving the voltage output while maintaining efficient charge collection.

3.12. Evaluation of materials designed as HTMs in perovskite solar cells

The comparative analysis of HOMO, LUMO, and bandgap (E_g) of our designed HTMs (BBT-Fx) and commonly used HTMs for PSCs is listed in Table S1. It appears that our designed materials stand out as promising candidates for use as HTM in PSCs. These materials exhibited moderate to slightly high HOMO values (–4.89 to –5.05 eV), which is close to the DFT calculated Spiro-OMeTAD value (–5.07 eV). Our HOMO values are also close to the experimental values of some commonly used HTMs such as PTAA (–5.10 eV), P3HT (–5.00 eV), and Spiro-OMeTAD (–5.20 eV), indicating good potential for hole transport. Moreover, their LUMO values are also well-aligned with the conduction band of perovskite materials such as $FAPbI_3$ (–4.00 eV), $MAPbI_3$ (–3.93 eV), and $MAPBr_3$ (–3.60 eV), indicating favorable electronic coupling for effective charge transfer. The HOMO-LUMO energy gap of our designed HTMs, ranging from 2.60 to 2.63 eV, are competitive and fall within the typical range for HTMs. The exciton binding energy results indicate that these materials are stable and favorable for practical applications. The reorganization energy, hole transfer integrals, and hole transfer rate suggest that they are efficient in terms of hole mobility. Overall, these materials are ideal nominees for HTMs and could be paired with widely used perovskite materials such as $FAPbI_3$ and $MAPbI_3$ to uplift the device's stability and efficiency.

4. Discussion

The present findings demonstrate that fluorinated benzodithiazole-based HTMs provide a useful molecular design strategy for tuning the electronic, optical, stability, and charge-transport properties required for perovskite solar cells. The combination of an electron-deficient BBT core with electron-rich TPA donor units creates a donor-acceptor framework that supports directional intramolecular charge transfer. Fluorination further adjusts the frontier orbital energies without disrupting the main hole-transport pathway. This is particularly important for HTMs because suitable HOMO alignment is required for efficient hole extraction from the perovskite absorber, while a sufficiently high LUMO level helps block electron leakage and suppress interfacial recombination.

The electronic and excited-state analyses consistently support the charge-separation ability of the designed BBT-Fx series. Compared with Spiro-OMeTAD, the designed HTMs show stronger charge-transfer character, lower exciton binding energies, and favorable donor-acceptor orbital separation. These features suggest that photo induced electron–hole pairs can be separated more easily, which is beneficial for reducing recombination losses at the perovskite/HTM interface. In terms of charge transport, BBT-F2 and BBT-F4 show particularly high hole-transfer rates due to stronger electronic coupling, indicating their potential advantage when fast hole hopping is the primary design target. In contrast, BBT-F6 exhibits the lowest hole reorganization energy, suggesting reduced structural relaxation during hole transport.

The stability-related descriptors also reveal a clear effect of fluorination. BBT-F6 shows the deepest HOMO level and the highest ionization potential among the designed molecules, indicating improved resistance toward oxidation. This is valuable because oxidative instability is one of the key limitations of organic HTMs during long-term device operation. The calculated solvation free energies and molecular electrostatic potential results further suggest that the fluorinated BBT derivatives may possess favorable interfacial interaction and film-forming behavior. Therefore, fluorination does not

simply shift the energy levels; it also contributes to improved chemical stability and molecular surface polarization, both of which are relevant for durable PSC performance.

The SCAPS-1D device simulations provide device-level support for the molecular-level results. Under identical simulation conditions, BBT-F6 delivers the best photovoltaic performance among the designed HTMs and slightly exceeds the simulated Spiro-OMeTAD reference in power conversion efficiency. This improvement mainly arises from enhanced voltage output and competitive fill factor rather than increased photocurrent, since the current density remains nearly unchanged across the simulated devices. However, these results should be interpreted as predictive rather than final proof. Experimental synthesis, film morphology analysis, hole mobility measurement, and full device fabrication are still required to confirm whether the calculated advantages of the BBT-Fx HTMs can be translated into real perovskite solar cell performance.

5. Conclusions

In this study, novel hole-transport materials based on a BBT core were designed by fluorinating the core; they were compared with the standard HTM Spiro-OMeTAD in terms of optoelectronic and photophysical properties. The HTMs are essential parts of perovskite solar cells, balancing perovskite absorbers by extracting holes while blocking electron flow to prevent recombination. They also provide essential protection against passive surface defects and moisture, ensuring high efficiency and stability. For this, the HOMO and LUMO levels of HTMs must be higher than the perovskite CBM and VBM, respectively, to efficiently extract holes and prevent electron backflow. Our DFT calculations validate appropriately aligned frontier orbitals and desirable energetic tuning: BBT-F2 and BBT-F4 possess HOMO energies of −4.89 eV, while further fluorination of the core to produce BBT-F6 results in additional HOMO stabilization to −5.05 eV, approaching that of Spiro-OMeTAD (−5.07 eV). LUMO energies are also pushed down to −2.27, −2.25, and −2.45 eV for BBT-F2, BBT-F4, and BBT-F6, respectively, relative to −1.97 eV for Spiro-OMeTAD. Optical simulations of these molecules dissolved in dichloromethane and chlorobenzene reveal that all three candidates feature absorption maxima around 400 nm, which should result in transparency across most of the visible spectrum and, therefore, little absorption overlap with the perovskite absorber. Computation of other electronic-stability descriptors revealed a similar story. The ionization potentials of 5.11 (BBT-F2), 5.10 (BBT-F4), and 5.22 eV (BBT-F6) demonstrate negligible changes from Spiro-OMeTAD (5.11 eV), though BBT-F6 is the most stabilized and, therefore, most oxidation-resistant fluorinated HTM.

The calculated Gibbs free energies in the range of −15.64 to −14.45 kcal mol^{-1} are significantly more negative than Spiro-OMeTAD (−13.43 kcal mol^{-1}), suggesting superior solvation and surface wetting properties. From charge-transport descriptors, the hole reorganization energy systematically decreases from 0.2576 (BBT-F2) to 0.2470 (BBT-F4) and to 0.2290 eV (BBT-F6), surpassing Spiro-OMeTAD (0.2476 eV). The computed hole-transfer rates still indicate fast hopping at 7.79×10^{13} (BBT-F2) and 8.82×10^{13} s^{-1} (BBT-F4), which greatly surpass 4.85×10^{12} s^{-1} (Spiro-OMeTAD). SCAPS-1D modeling confirms that the designed HTMs are competitive at the device level. A best-performing configuration delivered ~16% PCE, exceeding the simulated Spiro-OMeTAD baseline using the same architecture and input parameters. These results support further optimization and experimental validation of the proposed HTM design. Taken together, results suggest that BBT-F4 and BBT-F2 are promising candidates if high mobility is prioritized and demonstrate a facile route toward fluorinated HTMs with desirable properties, while BBT-F6 provides a route toward strongly stability-forward designs with the lowest HOMO and λ_{hole} of the series.

Use of AI tools declaration

The authors declare they have not used Artificial Intelligence (AI) tools in the creation of this article.

Acknowledgments

The authors acknowledge Jiangsu University of Science and Technology for partially supporting this work.

Conflict of interest

The authors declare no conflicts of interest.

Author contributions

S.A.S.: supervised the overall project, designed the work, edited the manuscript, and improved the final version; G.W. and R.S.: investigated, analyzed, interpreted the data, and wrote the manuscript; T.F.: contributed to figure preparation; O.C. and A.Y.: revised the final draft.

References

1. Marinova N, Valero S, Delgado JL (2017) Organic and perovskite solar cells: Working principles, materials and interfaces. *J Colloid Interface Sci* 488: 373–389. https://doi.org/10.1016/j.jcis.2016.11.021
2. Nelson J (2003) *The Physics of Solar Cells*, London: Imperial College Press. https://doi.org/10.1142/p276
3. Haider MDS, Hussain R, Kanwal N, et al. (2024) Enhancing PCE above 16.03% via linker engineering of donor layer: A DFT study of binary all-small-molecule organic solar cells. *Surf Interfaces* 55: 105434. https://doi.org/10.1016/j.surfin.2024.105434
4. Mohammad A, Shovon RB, Hasan MM, et al. (2024) Perovskite solar cell materials development for enhanced efficiency and stability. *Power Syst Technol* 48: 119–135. https://powertechjournal.com/index.php/journal/article/view/249
5. Saif AAA, Alahmadi G (2025) Optimization of HTL and ETL materials and parameters for high-efficiency $CH_3NH_3SnI_3$ perovskite solar cells. *AIMS Mater Sci* 12: 1004–1024. https://doi.org/10.3934/matersci.2025046
6. Ananthakumar S, Kumar JR, Babu SM (2019) Third-generation solar cells: Concept, materials and performance—An overview, In: Rajendran S, Naushad M, Raju K, et al. *Emerging Nanostructured Materials for Energy and Environmental Science. Environmental Chemistry for a Sustainable World*, Cham: Springer, 305–339. https://doi.org/10.1007/978-3-030-04474-9_7
7. Xie G, Xue Q, Ding H, et al. (2025) Management of intramolecular noncovalent interactions in dopant-free hole transport materials for high-performance perovskite solar cells. *Angew Chem Int Ed* 64: e202504144. https://doi.org/10.1002/anie.202504144
8. Shahzad N, Ishaq M, Laraib A, et al. (2026) Optimizing charge transport properties of dithieno[3,2-b:2′,3′-d]pyrrole-based hole transport materials for perovskite solar cells: A DFT study. *J Fluoresc* 36: 183–201. https://doi.org/10.1007/s10895-025-04565-8

9. Sharma D, Mehra R, Raj B (2022) Comparative study of hole transporting layers commonly used in high-efficiency perovskite solar cells. *J Mater Sci* 57: 21172–21191. https://doi.org/10.1007/s10853-022-07958-3
10. Zhong S, Yang Y, Wang Z, et al. (2026) Molecular tailoring of self-assembled monolayers derived from asymmetric benzothienoindole for efficient and stable inverted perovskite solar cells and modules. *Angew Chem Int Ed* 65: e1678852. https://doi.org/10.1002/anie.1678852
11. Arunkumar A, Ju XH (2024) Computational method on highly efficient D-π-A-π-D-based different molecular acceptors for organic solar cells applications and non-linear optical behaviour. *Spectrochim Acta A Mol Biomol Spectrosc* 317: 124391. https://doi.org/10.1016/j.saa.2024.124391
12. Arunkumar A, Anbarasan PM, Ju XH (2024) Acceptor tuned effect on the D-π-A-based organic efficient sensitizers for optoelectronic properties using quantum chemical study. *Opt Quantum Electron* 56: 520. https://doi.org/10.1007/s11082-023-06196-4
13. Yang Y, Yuan Q, Li H, et al. (2020) Dopant-free mixture of spiro-OMeTAD and PTAA with tunable wettability as hole transport layer enhancing performance of inverted $CsPbI_2Br$ perovskite solar cells. *Org Electron* 86: 105873. https://doi.org/10.1016/j.orgel.2020.105873
14. Nakka L, Cheng Y, Aberle AG, et al. (2022) Analytical review of spiro-OMeTAD hole transport materials: Paths toward stable and efficient perovskite solar cells. *Adv Energy Sustain Res* 3: 2200045. https://doi.org/10.1002/aesr.202200045
15. Xu D, Gong Z, Jiang Y, et al. (2022) Constructing molecular bridge for high-efficiency and stable perovskite solar cells based on P3HT. *Nat Commun* 13: 7020. https://doi.org/10.1038/s41467-022-34768-7
16. Anrango-Camacho C, Pavón-Ipiales K, Frontana-Uribe BA, et al. (2022) Recent advances in hole-transporting layers for organic solar cells. *Nanomaterials* 12: 443. https://doi.org/10.3390/nano12030443
17. Muniandy S, Idris MIB, Napiah ZAFM, et al. (2021) An investigation on NiO for hole transport material in perovskite solar cells. 2021 IEEE Regional Symposium on Micro and Nanoelectronics (RSM), Kuala Lumpur, Malaysia, 112–115. https://doi.org/10.1109/RSM52397.2021.9511573
18. Shah SA, Sayyar R, Zou X, et al. (2026) Theoretical study on the optoelectronics and charge transport properties of difluoro benzothiadiazole-based hole transport materials for perovskite solar cells. *J Fluoresc* 36: 2661–2678. https://doi.org/10.1007/s10895-026-04722-7
19. Dennington R, Keith TA, Millam JM (2016) GaussView, version 6.0.16. Semichem Inc, Shawnee Mission, KS, USA. https://gaussian.com/gaussview6/
20. Becke AD (1993) Density-functional thermochemistry. III. The role of exact exchange. *J Chem Phys* 98: 5648–5652. https://doi.org/10.1063/1.464913
21. Chi WJ, Li QS, Li ZS (2016) Exploring the electrochemical properties of hole transport materials with spiro-cores for efficient perovskite solar cells from first-principles. *Nanoscale* 8: 6146–6154. https://doi.org/10.1039/C6NR00235H
22. Cancès E, Mennucci B, Tomasi J (1997) A new integral equation formalism for the polarizable continuum model: Theoretical background and applications to isotropic and anisotropic dielectrics. *J Chem Phys* 107: 3032–3041. https://doi.org/10.1063/1.474659
23. Yanai T, Tew DP, Handy NC (2004) A new hybrid exchange–correlation functional using the Coulomb-attenuating method (CAM-B3LYP). *Chem Phys Lett* 393: 51–57. https://doi.org/10.1016/j.cplett.2004.06.011

24. Yang LN, Chen SL, Li ZS (2015) How does the silicon element perform in JD-dyes: A theoretical investigation. *J Mater Chem A* 3: 8308–8315. https://doi.org/10.1039/C5TA00812C
25. Sun ZZ, Feng S, Gu C, et al. (2019) Probing effects of molecular conformation on the electronic and charge transport properties in two- and three-dimensional small molecule hole-transporting materials: A theoretical investigation. *Phys Chem Chem Phys* 21: 15206–15214. https://doi.org/10.1039/C9CP01986C
26. Lu T, Chen F (2012) Multiwfn: A multifunctional wavefunction analyzer. *J Comput Chem* 33: 580–592. https://doi.org/10.1002/jcc.22885
27. Wang Y, Verma P, Zhang L, et al. (2020) M06-SX screened-exchange density functional for chemistry and solid-state physics. *Proc Natl Acad Sci USA* 117: 2294–2301. https://doi.org/10.1073/pnas.1913699117
28. Park NG (2015) Perovskite solar cells: An emerging photovoltaic technology. *Mater Today* 18: 65–72. https://doi.org/10.1016/j.mattod.2014.07.007
29. Shahzad N, Chatha SAS, Iqbal J, et al. (2024) Enhancing perovskite solar cells performance through tailored design: pyridine-functionalized phenothiazine derivatives with modified end-capped acceptor moieties. *Eng Res Express* 6: 045316. https://doi.org/10.1088/2631-8695/ad82a8
30. Shao S, Loi MA (2020) The role of the interfaces in perovskite solar cells. *Adv Mater Interfaces* 7: 1901469. https://doi.org/10.1002/admi.201901469
31. Achoi MF, Kato S, Kishi N, et al. (2024) Improved photovoltaic properties of $((CH_3NH_3)_{1-x}Cs_x)_3Bi_2I_9$: (x = 0–1.0) hybrid perovskite solar cells via a hot immersion method. *AIMS Mater Sci* 11: 605–619. https://doi.org/10.3934/matersci.2024031
32. Fatima T, Bibi S, Muhammad S, et al. (2025) Systematic computational designing of efficient phenalene and pyrene based derivatives to tune the optical and nonlinear optical response. *J Fluoresc* 35: 10987–11006. https://doi.org/10.1007/s10895-025-04330-x
33. Ameen S, Rub MA, Kosa SA, et al. (2016) Perovskite solar cells: Influence of hole transporting materials on power conversion efficiency. *ChemSusChem* 9: 10–27. https://doi.org/10.1002/cssc.201501228
34. Xia Z, Zhang J, Gao X, et al. (2021) Fine-tuning the dipole moment of asymmetric non-fullerene acceptors enabling efficient and stable organic solar cells. *ACS Appl Mater Interfaces* 13: 23983–23992. https://doi.org/10.1021/acsami.1c02652
35. Zhang Y, Wang L, Mao L, et al. (2020) Carbazole-substituted NP-based derivative as hole transporting material for highly efficient perovskite solar cells. *Spectrochim Acta A Mol Biomol Spectrosc* 228: 117808. https://doi.org/10.1016/j.saa.2019.117808
36. Shahzad N, Fatima R, Etabti H, et al. (2025) Quantum design and investigation of dibenzo[g,p]chrysene-based hole transport materials for efficient perovskite solar cells. *Sol Energy* 301: 113980. https://doi.org/10.1016/j.solener.2025.113980
37. Bernazzani L, Duce C, Micheli A, et al. (2006) Predicting physical–chemical properties of compounds from molecular structures by recursive neural networks. *J Chem Inf Model* 46: 2030–2042. https://doi.org/10.1021/ci060104e
38. Akram SJ, Iqbal J, Ans M, et al. (2022) Designing of the indacenodithiophene core-based small molecules for optoelectronic applications: A DFT approach. *Sol Energy* 237: 108–121. https://doi.org/10.1016/j.solener.2022.03.072

39. Lu C, Paramasivam M, Park K, et al. (2019) Phenothiazine functionalized multifunctional A–π–D–π–D–π–A-type hole-transporting materials via sequential C–H arylation approach for efficient and stable perovskite solar cells. *ACS Appl Mater Interfaces* 11: 14011–14022. https://doi.org/10.1021/acsami.8b20646
40. Cowan SR, Banerji N, Leong WL, et al. (2012) Charge formation, recombination, and sweep-out dynamics in organic solar cells. *Adv Funct Mater* 22: 1116–1128. https://doi.org/10.1002/adfm.201101632
41. Bi D, Yang L, Boschloo G, et al. (2013) Effect of different hole transport materials on recombination in $CH_3NH_3PbI_3$ perovskite-sensitized mesoscopic solar cells. *J Phys Chem Lett* 4: 1532–1536. https://doi.org/10.1021/jz400638x
42. Koster LJA, Shaheen SE, Hummelen JC (2012) Pathways to a new efficiency regime for organic solar cells. *Adv Energy Mater* 2: 1246–1253. https://doi.org/10.1002/aenm.201200103
43. Marcus RA (1964) Chemical and electrochemical electron-transfer theory. *Annu Rev Phys Chem* 15: 155–196. https://doi.org/10.1146/annurev.pc.15.100164.001103
44. Padmanabhan J, Arif Z, Singh P, et al. (2021) Chemical reactivity and skin sensitization studies on a series of chloro- and fluoropyrroles—A computational approach. *ACS Omega* 6: 21514–21524. https://doi.org/10.1021/acsomega.1c02436
45. Li HX, Zheng RH, Shi Q (2011) Theoretical study on charge carrier mobilities of tetrathiafulvalene derivatives. *Phys Chem Chem Phys* 13: 5642–5650. https://doi.org/10.1039/C0CP01016B
46. Imahori H, Kobori Y, Kaji H (2021) Manipulation of charge-transfer states by molecular design: Perspective from "dynamic exciton". *Acc Mater Res* 2: 501–514. https://doi.org/10.1021/accountsmr.1c00045
47. Akram W, Zahid WA, Abu El Maati L, et al. (2023) Engineering push–pull structural versatility in highly functional carbazole-based hole transporting materials design for efficient perovskites solar devices. *J Photochem Photobiol A Chem* 444: 114991. https://doi.org/10.1016/j.jphotochem.2023.114991
48. Spackman MA, Jayatilaka D (2009) Hirshfeld surface analysis. *CrystEngComm* 11: 19–32. https://doi.org/10.1039/B818330A
49. Hirshfeld FL (1977) Bonded-atom fragments for describing molecular charge densities. *Theor Chim Acta* 44: 129–138. https://doi.org/10.1007/BF00549096
50. McKinnon JJ, Jayatilaka D, Spackman MA (2007) Towards quantitative analysis of intermolecular interactions with Hirshfeld surfaces. *Chem Commun* 2007: 3814–3816. https://doi.org/10.1039/B704980C
51. Seth SK, Maity GC, Kar T (2011) Structural elucidation, Hirshfeld surface analysis and quantum mechanical study of para-nitro benzylidene methyl arjunolate. *J Mol Struct* 1000: 120–126. https://doi.org/10.1016/j.molstruc.2011.06.003
52. Abad N, Sallam HH, Al-Ostoot FH, et al. (2021) Synthesis, crystal structure, DFT calculations, Hirshfeld surface analysis, energy frameworks, molecular dynamics and docking studies of novel isoxazolequinoxaline derivative (IZQ) as anti-cancer drug. *J Mol Struct* 1232: 130004. https://doi.org/10.1016/j.molstruc.2021.130004
53. Burgelman M, Nollet P, Degrave S (2000) Modelling polycrystalline semiconductor solar cells. *Thin Solid Films* 361–362: 527–532. https://doi.org/10.1016/S0040-6090(99)00825-1

54. Singh NK, Agarwal A, Singh AK, et al. (2024) Design and performance evaluation of eco-friendly $FASnI_3/CsSn_{0.5}Ge_{0.5}I_3$ based perovskite solar cell with distinct charge transport layer: A computational modeling. *Sol Energy* 268: 112256. https://doi.org/10.1016/j.solener.2023.112256
55. Benami A, Ouslimane T, Et-taya L, et al. (2022) Comparison of the effects of ZnO and TiO_2 on the performance of perovskite solar cells via SCAPS-1D software package. *J Nano Electron Phys* 14: 01033. https://doi.org/10.21272/jnep.14(1).01033
56. Targhi FF, Jalili YS, Kanjouri F (2018) $MAPbI_3$ and $FAPbI_3$ perovskites as solar cells: Case study on structural, electrical and optical properties. *Results Phys* 10: 616–627. https://doi.org/10.1016/j.rinp.2018.07.007
57. Duan C, Zhang X, Du Z, et al. (2023) Perovskite interface defect passivation with poly(ethylene oxide) for improving power conversion efficiency of the inverted solar cells. *Opt Express* 31: 20364–20376. https://doi.org/10.1364/OE.489290
58. Salem AF, El-Bashar R, El-Rabaie SM, et al. (2024) Nanoscale grating-based perovskite solar cell with improved efficiency. *Phys Scr* 99: 115504. https://doi.org/10.1088/1402-4896/ad7dc1
59. Manzoor S, Abbas F, Munir R, et al. (2025) Theoretical investigation of hole transport and donor materials derived from anthracene with improved optoelectronic characteristics for perovskite and organic solar cell applications. *Opt Quantum Electron* 57: 509. https://doi.org/10.1007/s11082-025-08429-0



AIMS Press

© 2026 the Author(s), licensee AIMS Press. This is an open access article distributed under the terms of the Creative Commons Attribution License (http://creativecommons.org/licenses/by/4.0)